MSU Jumper: A Single-Motor-Actuated Miniature Steerable Jumping Robot

Jianguo Zhao, *Student Member, IEEE*, Jing Xu, *Member, IEEE*, Bingtuan Gao, *Member, IEEE*, Ning Xi, *Fellow, IEEE*, Fernando J. Cintrón, *Student Member, IEEE*, Matt W. Mutka, *Fellow, IEEE*, and Li Xiao, *Senior Member, IEEE*

***Abstract*—The ability to jump is found widely among small animals such as frogs, grasshoppers, and fleas. They jump to overcome large obstacles relative to their small sizes. Inspired by the animals' jumping capability, a miniature jumping robot—Michigan State University (MSU) Jumper—has been developed. In this paper, the mechanical design, fabrication, and experimentation of the MSU jumper are presented. The robot can achieve the following three performances simultaneously, which distinguish it from the other existing jumping robots. First, it can perform continuous steerable jumping that is based on the self-righting and the steering capabilities. Second, the robot only requires a single actuator to perform all the functions. Third, the robot has a light weight (23.5 g) to reduce the damage that results from the impact of landing. Experimental results show that, with a 75° take-off angle, the robot can jump up to 87 cm in vertical height and 90 cm in horizontal distance. The robot has a wide range of applications such as sensor/communication networks, search and rescue, surveillance, and environmental monitoring.**

***Index Terms*—Biologically inspired robot, jumping robot, mechanism design, miniature robot, sensor network.**

I. Introduction

With the advancement of electronic and networking technology, it is possible to build small and inexpensive wireless sensors that can form a wireless sensor network to acquire useful information from the environment. In such a network, only a limited number of sensors can be used; therefore, it is important to deploy them appropriately to obtain the best data acquisition result [1]. Instead of deploying them manually, one can equip the sensors with the locomotion ability so that they can deploy themselves to form a mobile sensor network.

There are three reasons to employ jumping as a locomotion method for mobile sensors. First, jumping enables a sensor to overcome a large obstacle in comparison with its size. In fact, the ratio between the jumping height and the sensor size can be 30 [2]. In contrast, wheeled locomotion on land cannot overcome obstacles that are larger than the wheel diameter. For example, the Mars rover, even with a special rocker-bogie suspension system, can only overcome obstacles with sizes at most 1.5 times the wheel diameter [3]. Second, jumping provides the best tradeoff between the locomotion efficacy (height per gait) and the energy efficiency (energy per meter) among various locomotion methods such as walking, running, or wheeled locomotion [4]. Third, the wireless transmission range increases when the sensor jumps into the air [5]. As shown in [6], when one sensor is elevated 1 m above the ground, the communication range is about six times the range when both sensors are placed on the ground. For these reasons, we investigate how to equip sensors with the jumping ability in this paper. Since mobile sensors can be considered as robots, we will use the word "robot" in the following discussions.

Researchers have built many robots with the jumping ability in the past decade, and there exist several doctoral dissertations for this topic [7]–[9]. All of the existing designs accomplish jumping by an instant release of the energy that is stored in the robot. As a result, we can classify all of the robots with the jumping ability by their energy storage methods.

The most popular method to store energy is based on traditional springs such as compression, extension, or torsion springs. The frogbot stores and releases the energy in an extension spring through a geared six-bar mechanism [3]. The old surveillance robot has a jumping mechanism similar to the frogbot [10], while the new one switches to a torsion spring-actuated four-bar mechanism [11]. The intermittent hopping robot also employs a geared six-bar mechanism for jumping [12]. The mini-whegs utilizes a slip gear system to store and release the energy in an extension spring via a four-bar mechanism [13]. With torsion springs, a jumping robot for Mars exploration is designed with a novel cylindrical scissor mechanism [14]. The old Grillo robot employs a motor-driven eccentric cam to charge a torsion spring that actuates the rear legs [15]; the new prototype switches to two extension harmonic-wire springs [16], [17]. The wheel-based stair-climbing robot with a soft landing ability is based on four compression springs [18]. The EPFL jumper V1

Manuscript received July 24, 2012; revised December 2, 2012; accepted February 21, 2013. Date of publication March 18, 2013; date of current version June 3, 2013. This paper was recommended for publication by Associate Editor Y. Choi and Editor J.-P. Laumond upon evaluation of the reviewers' comments. This work was supported in part by the National Science Foundation under Grant CNS-0721441, in part by the U.S. Army Research Laboratory, and in part by the U. S. Army Research Office under Grant W911NF-09-1-0321 and Grant W911NF-10-1-0358.

J. Zhao and N. Xi are with the Department of Electrical and Computer Engineering, Michigan State University, East Lansing, MI 48824 USA (e-mail: zhaojia1@msu.edu; xin@egr.msu.edu).

J. Xu is with the Department of Precision Instruments and Mechanology, Tsinghua University, Beijing, 100084 China (e-mail: jingxu@mail.tsinghua.edu.cn).

B. Gao is with the School of Electrical Engineering, Southeast University, Nanjing, 210096 China (e-mail: gaobingtuan@seu.edu.cn).

F. J. Cintrón, M. W. Mutka, and L. Xiao are with the Department of Computer Science and Engineering, Michigan State University, East Lansing, MI 48824 USA (e-mail: cintrong@cse.msu.edu; mutka@cse.msu.edu; lxiao@cse.msu.edu).

This paper has supplementary downloadable material available at http://ieeexplore.ieee.org.

Color versions of one or more of the figures in this paper are available online at http://ieeexplore.ieee.org.

Digital Object Identifier 10.1109/TRO.2013.2249371

can achieve a jumping height of about 1.4 m with torsion springs charged and released by a motor-driven cam system [19]. This robot is later improved to add the self-recovery capability [20] and the jumping direction changing ability [21]. The multimodal robot can jump up to 1.7 m based on two symmetrical extension spring-actuated four-bar mechanisms [22]. Our first generation jumping robot relies on compression springs [23], and the second one employs torsion springs [24].

The elastic elements, or customized special springs, are the second method for energy storage. The scout robot employs a motor-driven winch to charge a single bending plate spring and release it to directly strike the ground for jumping [25]. The compact jumping robot utilizes an elastic strip to form closed elastica actuated by two revolute joints [26], [27]. The MIT microbot charges the energy to two symmetrical carbon fiber strips with dielectric elastomer actuators (DEA) [28], [29]. The Jollbot, with a spherical structure formed by several metal semicircular hoops, deforms the spherical shape to store energy [30]. A similar idea is utilized in the deformable robot, but the hoop material is replaced by shape memory alloy (SMA) [31], [32]. The flea robot also uses SMA to actuate a four-bar mechanism for jumping [2]. The mesoscale jumping robot employs the SMA as a special spring to implement the jumping mechanism as well [33].

The third method to store energy for jumping is based on compressed air. In this method, the robot carries an air tank and a pneumatic cylinder. The sudden release of air in the tank forces the cylinder to extend. The rescue robot [34], [35] and the patrol robot [36] employ the cylinder's extension to strike the ground for jumping. Instead of striking the ground, the quadruped Airhopper accomplishes jumping with several cylinder-actuated four-bar mechanisms [37], [38]. With a biped structure, the Mowgli robot—different from other pneumatic-based jumping robots—uses several pneumatic artificial muscles for jumping [39].

In addition to the aforementioned three methods, several other approaches exist. The pendulum jumping machine generates energy for jumping from the swing of arms [40]. The jumping robot developed by the Sandia National Labs [41], and recently improved by Boston Dynamics [42], uses the energy from hydrocarbon fuels and can achieve the largest jumping height to date. The robot based on microelectromechanical technology is the smallest jumping robot in the literature [43], [44]. The voice coil actuator-based robot charges energy into an electrical capacitor instead of a mechanical structure [45].

For the sensor network application, the design requirements of our robot are different from existing robots. The detailed requirements can be summarized in three aspects. First, to make jumping a valid locomotion method, the robot should be able to perform continuous steerable jumping. Toward this goal, the robot should have multiple functions, which include jumping, self-righting from the landing position, and changing the jumping direction—steering. Second, we aim to accomplish the multiple functions with the minimum number of actuators. Minimum actuator design can reduce the robot's weight, thereby improving the robot's jumping performance. Third, the robot's weight should be light. Specifically, the mass should be less than 30 g. With a light weight, each jump consumes less energy for the same jumping height, which can increase the jumping times due to the robot's limited energy supply. Moreover, a lightweight robot is less susceptible to the damage from the impact of landing.

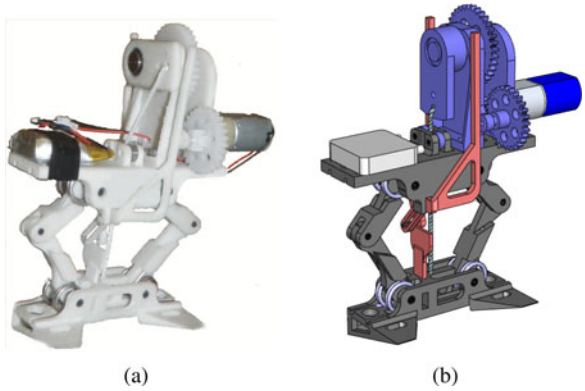

Fig. 1. MSU jumper: (a) prototype and (b) solid model.

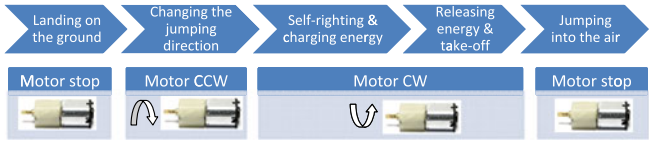

Fig. 2. Jumping motion sequence with the corresponding motor rotation directions.

Initially, we chose good jumping performances to be a design priority instead of the minimum number of actuators. After further investigation, however, we switched to minimizing the number of actuators to be a priority because it would lead to better jumping performances. Suppose the design for each mechanism in the robot is fixed. Compared with the case of actuating each mechanism with one motor, the robot's weight decreases if a single motor is employed to actuate all of the mechanisms. As a result, the jumping performance improves.

The robot described in this paper—with the prototype and solid model shown in Fig. 1—can fulfill the three design goals. First, it can perform continuous steerable jumping with four mechanisms for four functions. In fact, the robot can achieve the motion sequence shown in the upper row of Fig. 2. After the robot lands on the ground, it steers to the desired jumping direction. Then, it charges the energy and performs the self-righting at the same time. After the energy is fully charged, the robot releases the energy and leaps into the air. Second, a single motor is employed to achieve the motion sequence in Fig. 2. The motor's two direction rotations [clockwise (CW) and counter clockwise (CCW)] actuate different functions as shown in the bottom row of Fig. 2. Third, the goal of small weight is accomplished with the robot having a mass of 23.5 g.

The most relevant research in existing jumping robots is the frogbot [3] for celestial exploration. It can achieve continuous steerable jumping with a single motor. Moreover, the robot has impressive jumping performances: 90 cm in height and 200 cm in distance. Nevertheless, the major difference between the

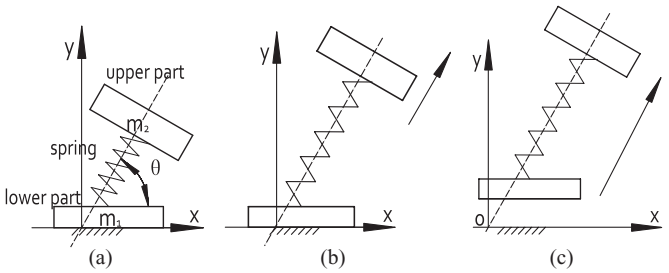

Fig. 3. Jumping principle for spring-based jumping robots.

frogbot and our robot is the different targeting weight ranges. The frogbot has a mass of 1300 g, while our robot is designed to be less than 30 g. The smaller weight constrains the mechanism design for each function; consequently, the designs for all of the mechanisms are different. We will discuss such differences for each mechanism in detail in Section III.

The EPFL jumper V3 is another close research [21]. It can perform continuous steerable jumping with a small mass of 14.33 g. With the light weight, good jumping performances can still be achieved: 62 cm in height and 46 cm in distance. The major difference between our robot and the EPFL jumper V3 is that the minimum actuation strategy is pursued in our robot, which leads to different designs for each mechanism that will be discussed in Section III as well.

The major contribution of this paper is the design and development of a new jumping robot that satisfies the three design requirements: continuous steerable jumping, minimum actuation, and light weight. Although some robots can fulfill two of the three requirements, no robot can satisfy all of the three requirements to the best of our knowledge.

The rest of this paper is organized as follows. We discuss the mathematical model of the jumping process in Section II. After that, we elaborate the mechanical design for the four mechanisms in Section III. Then, we perform the optimal design to obtain the best mechanism dimensions in Section IV. Finally, we present the implementation details, experimental results, and comparison with existing jumping robots in Section V.

II. Modeling of the Jumping Process

Animals with the jumping ability utilize the same jumping principle. At first, their bodies accelerate upward while their feet remain on the ground. Once the bodies reach some height, they bring the feet to leave the ground, and the animals thrust into the air [47]. With the same principle, a simplified robotic model can be established as shown in Fig. 3(a). The robot contains an upper part and a lower part connected by an energy storage medium shown as a spring in the figure. In this section, the theoretical jumping performance will be analyzed based on this model.

With the simplified model, the jumping process can be divided into two steps as shown in Fig. 3. The first step, spanning from (a) to (b), starts once the energy that is stored in the spring is released and ends before the robot leaves the ground. In this step, the upper part first accelerates upward due to the spring force, while the lower part remains stationary. Once the upper part moves to a specific height, a perfect inelastic collision happens between the two parts if the spring constant is large [23]. After the collision, both parts have the same velocity, which is the robot's take-off velocity.

Let the mass for the upper and lower part be m_2 and m_1, respectively. In the ideal case, all the energy E_0 stored in the spring is converted to the kinetic energy of the upper part. Therefore, the speed of the upper part before the inelastic collision is $v_2 = \sqrt{2E_0/m_2}$. Let the take-off velocity be v_0; then we have $m_2 v_2 = (m_1 + m_2)v_0$ by the conservation of momentum, and v_0 can be solved as

$$v_0 = \frac{m_2}{m_1 + m_2} v_2 = \frac{\sqrt{2m_2 E_0}}{m_1 + m_2}. \tag{1}$$

Thus, the kinetic energy at take-off is

$$E = \frac{1}{2}(m_1 + m_2)v_0^2 = \frac{m_2}{m_1 + m_2} E_0 = \frac{1}{r+1} E_0$$

where $r = m_1/m_2$ is the mass ratio between the lower and upper part.

The second step, spanning from Fig. 3(b) to (c), begins when the robot leaves the ground with the take-off speed v_0 and ends when it lands on the ground. The robot in the air will be subject to the gravitational force and the air resistance. If the latter is negligible, then the robot performs a projectile motion. We establish a coordinate frame with the origin at the take-off point, the x-axis along the horizontal direction, and the y-axis along the vertical direction; then the robot's trajectory is

$$x(t) = v_0 t \cos\theta, \quad y(t) = v_0 t \sin\theta - \frac{1}{2} g t^2 \tag{2}$$

where θ is the take-off angle and g is the gravitational constant. Based on the trajectory, the jumping height h and distance d can be obtained as

$$h = \frac{v_0^2}{2g} \sin^2\theta = \frac{E_0 \sin^2\theta}{(1+r)mg} \tag{3}$$

$$d = \frac{v_0^2}{g} \sin 2\theta = \frac{2E_0 \sin 2\theta}{(1+r)mg} \tag{4}$$

where $m = m_1 + m_2$ is the robot's total mass. From these equations, we see that in order to maximize the jumping height and distance, the mass ratio r and the total mass m should be minimized, while the stored energy E_0 should be maximized. In addition, the jumping height and distance vary with the take-off angle.

If the air resistance is not negligible, then an additional drag force should be considered. The drag force for a rigid body moving with velocity v and frontal area A is $F_{\mathrm{drag}} = C_d \rho A v^2/2$, where C_d is the drag coefficient related to the robot's shape, and ρ is the air density [48]. Therefore, the equation of motion for the robot is

$$m\ddot{x}(t) + \frac{1}{2} C_d \rho A_x(t) \dot{x}(t)^2 = 0 \tag{5}$$

$$m\ddot{y}(t) + \frac{1}{2} C_d \rho A_y(t) \dot{y}(t)^2 + mg = 0 \tag{6}$$

where $A_x(t)$ and $A_y(t)$ are the frontal areas perpendicular to the x- and y-axes, respectively. $A_x(t)$ and $A_y(t)$ vary with time

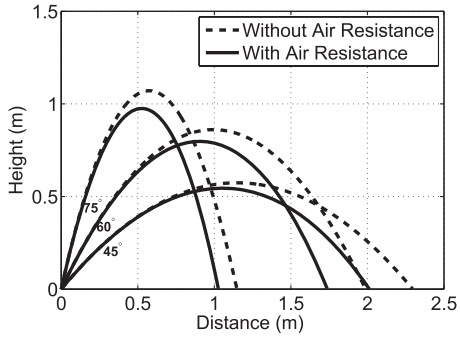

Fig. 4. Theoretical jumping trajectories for different take-off angles.

since the robot may change its orientation in the air. The detailed investigation of such a change, however, is quite complicated because it depends on the robot's unknown angular momentum during take-off [49]. For simplicity, we assume that $A_x(t) = A_x$ and $A_y(t) = A_y$ are constants, which will not affect the final results much since the drag force is usually very small.

Given the initial condition as $x(0) = 0$, $y(0) = 0$, $\dot{x}(0) = v_0 \cos\theta$, and $\dot{y}(0) = v_0 \sin\theta$, the robot's trajectory is governed by the solution to (5) and (6) as follows [7]:

$$x(t) = \frac{1}{M} \ln(1 + v_0 M t \cos\theta) \tag{7}$$

$$y(t) = \frac{1}{N} \ln[\cos(\sqrt{Ng}t) + L \sin(\sqrt{Ng}t)] \tag{8}$$

where $M = C_d \rho A_x/(2m)$, $N = C_d \rho A_y/(2m)$, and $L = v_0 \sin\theta\sqrt{N/g}$. The jumping performance with the air resistance can be derived from $x(t)$ and $y(t)$ as [7]

$$h = \frac{1}{N} \ln(\sqrt{1 + L^2}) \tag{9}$$

$$d = \frac{1}{M} \ln\left[1 + v_0 \cos\theta \frac{M}{\sqrt{Ng}} \arccos\left(\frac{1 - L^2}{1 + L^2}\right)\right] \tag{10}$$

Based on the previous analysis, theoretical jumping performances without and with the air resistance can be obtained. According to our previous design [46], the following parameters are used for calculation: $E_0 = 0.3\,\text{J}$, $m_1 = 5\,\text{g}$, $m_2 = 15\,\text{g}$, $C_d = 1.58$, $\rho = 1.2\,\text{kg/m}^3$, and $A_x = A_y = 2000\,\text{mm}^2$ for three different take-off angles: 75°, 60°, and 45°. C_d is chosen as the maximum value for the insect experiment in [50] to obtain a conservative result. With the aforementioned parameters, the theoretical jumping trajectories for the three take-off angles are obtained and plotted in Fig. 4. The angle 75° is chosen as the take-off angle for our robot because the jumping distance and height at this angle are approximately the same. In this case, the robot can overcome obstacles as large as possible without sacrificing the horizontal locomotion ability.

The jumping model presented in this section will also be used to derive the theoretical performance for the robot prototype to compare with the experimental results in Section V.

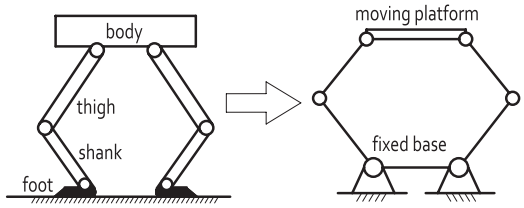

Fig. 5. Jumping mechanism synthesis.

III. Mechanical Design and Analysis

Four mechanisms realize the jumping motion sequence in Fig. 2. First, the jumping mechanism transforms the stored energy into the robot's kinetic energy for take-off. Second, the energy mechanism charges the energy and releases it instantly. Third, the self-righting mechanism can have the robot stand up after it lands on the ground. Fourth, the steering mechanism changes the robot's jumping direction. The four mechanisms will be described and analyzed in detail in this section.

A. Jumping Mechanism

For the jumping mechanism, we choose springs as the energy storage medium since 1) they can be implemented with a small weight; 2) they can be obtained easily at a low cost since they are off-the-shelf components; and 3) good jumping performances can be achieved [19], [22].

To accomplish jumping with springs, some robots directly strike the ground using springs such as the scout robot [25] and the MIT microbot [29]. This method, however, may lead to the robot's premature take-off from the ground before the energy stored in springs is fully released. Other robots employ spring-actuated four or six-bar mechanisms to achieve jumping such as the EPFL jumper V1 [19] and the frogbot [3], which can solve the premature take-off problem.

Various animals with the jumping ability—such as humans, frogs, locusts, or fleas—achieve jumping by extending a pair of legs. The vertical jumping can be modeled as shown on the left of Fig. 5, where the leg is divided into three parts: the upper leg (thigh), the lower leg (shank), and the foot [51]. We assume that each pair of adjacent parts is connected by a revolute joint since they can rotate relative to each other. Moreover, since both feet stay on the ground before take-off, they can be considered as one part. Therefore, jumping can be emulated by a planar parallel mechanism with two feet as the fixed base, the body as the moving platform, and the two legs as the kinematic chains connecting the platform to the base. This mechanism, which is shown on the right of Fig. 5, is chosen as the jumping mechanism for our robot.

A detailed schematic for the jumping mechanism is shown in Fig. 6(a). The mechanism is symmetric with respect to the vertical line OO′. Six revolute joints are placed at A, B, C, D, E, and F. We establish a coordinate frame with the X-axis along $\overrightarrow{\text{ED}}$ and the Y-axis along $\overrightarrow{\text{OO}'}$. Denote the link length as $|\text{AB}| = l_1$, $|\text{BC}| = |\text{AF}| = l_2$, $|\text{CD}| = |\text{FE}| = l_3$, and $|\text{DE}| = l_4$. Denote the vertical distance between AB and ED as y, the angle between $\overrightarrow{\text{BA}}$ and $\overrightarrow{\text{AF}}$ as α, and the angle between $\overrightarrow{\text{DE}}$ and $\overrightarrow{\text{EF}}$ as β. Eight

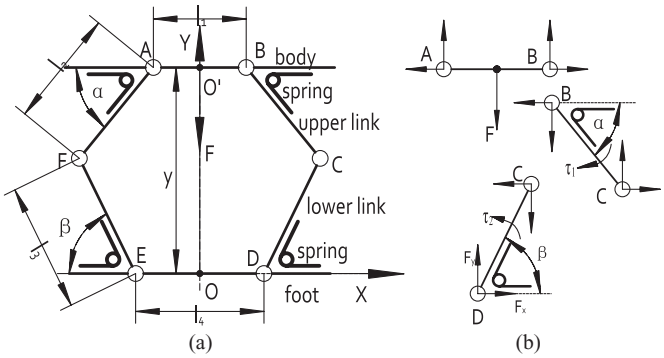

Fig. 6. Schematic of the jumping mechanism. (a) Jumping mechanism. (b) Static analysis for the right side part.

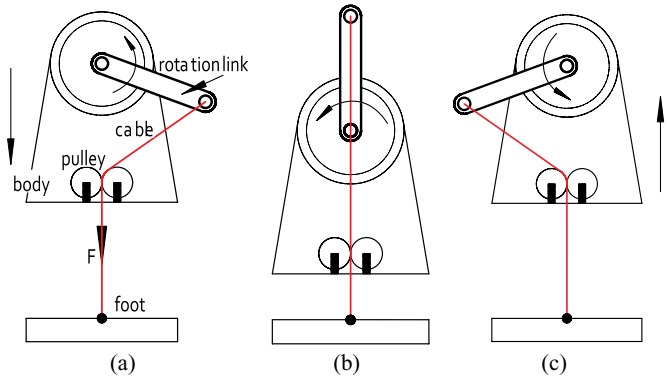

Fig. 7. Energy mechanism. (a) Intermediate position during the charge of energy. (b) Critical position. (c) Intermediate position during the release of energy.

torsion springs with a spring constant k are placed at A, B, E, and D—two springs for each place. This way, the springs can be charged to store energy if a vertical downward force F is applied at point O′, and the energy can be released once F is removed.

The jumping mechanism is different from the one used in the frogbot [3] in two aspects, although both belong to the category of six-bar mechanisms. On one hand, a linear extension spring is employed in the frogbot, while torsion springs are used in our robot. On the other hand, different methods are utilized to make the body only move vertically with respect to the foot. The frogbot employs two pairs of gears at both the body and the foot, while our robot relies on the symmetric placement of torsion springs.

For the mechanism optimization in Section IV, we analyze the statics for the required force F—which varies with distance y—to charge the energy. Since the mechanism is symmetric with respect to OO′, analysis for the right-side part is sufficient. Fig. 6(b) shows the free body diagrams for links AB, BC, and CD, where all forces are decomposed along the coordinate frame axes. The component forces along the same axis, except F, have the same quantity, although the directions may be opposite. Denote the same quantity as F_x and F_y along the x-axis and y-axis, respectively. From the figure, the static equations for the three links are

$$\begin{aligned} F &= 2F_y \\ \tau_1 = 2k\left(\frac{\pi}{2}-\alpha\right) &= F_x l_2 \sin\alpha + F_y l_2 \cos\alpha \\ \tau_2 = 2k\left(\frac{\pi}{2}-\beta\right) &= -F_x l_3 \sin\beta + F_y l_3 \cos\beta \end{aligned}$$

where τ_1 and τ_2 are the torques generated by the springs. From the previous equations, F can be solved as

$$F = \frac{2kl_3(\pi-2\alpha)\sin\beta + 2kl_2(\pi-2\beta)\sin\alpha}{l_2 l_3 \sin(\alpha+\beta)} \tag{11}$$

Note that α and β are the functions of y and point C's vertical coordinates y_C. Point C is the intersection point of two circles with centers at B : $(l_1/2,\ y)$ and D : $(l_4/2,\ 0)$; therefore, y_C can be solved as

$$y_C = \frac{y}{2} - \frac{y(l_2^2-l_3^2)}{2e} + \frac{l_d}{4e}\sqrt{[(l_2+l_3)^2-e][e-(l_2-l_3)^2]} \tag{12}$$

where $e = l_d^2/4 + y^2$ with $l_d = l_4 - l_1$. In fact, there are two intersection points for those two circles, but the point corresponding to the configuration shown in Fig. 6(a) is unique. Once y_C is obtained, we can solve α and β as

$$\alpha = \arcsin\frac{y-y_C}{l_2}, \quad \beta = \arcsin\frac{y_C}{l_3} \tag{13}$$

Substituting (12) and (13) into (11), we can express F to be a function of y by eliminating α, β, and y_C.

To facilitate the optimization in Section IV, let $y_{\max}$ and $y_{\min}$ be the maximum and minimum value of y. The largest value for $y_{\max}$ is $\sqrt{(l_2+l_3)^2 - l_d^2/4}$ when AF and FE, BC and CD are collinear. However, we cannot achieve this value because it corresponds to the singular configuration which we should stay clear. Meanwhile, $y_{\max}$ should be as large as possible so that the energy stored in the spring can be released thoroughly. To simplify the design process, we empirically let

$$y_{\max} = 0.95\sqrt{(l_2+l_3)^2 - l_d^2/4} \tag{14}$$

B. Energy Mechanism

For the jumping mechanism, another energy mechanism is required to store energy and release it when necessary. Generally, this can be achieved in two ways. The first approach rotates the motor in one direction to charge energy and in the other direction to release energy. Examples include the scout robot [25] and our second robot [24]. The second approach rotates the motor in a single direction for energy charge and release, leading to a short cycle time. This can be achieved by a slip-gear system [10], [13], an eccentric cam [15], [19], or a variable length crank mechanism [30]. To obtain a short-cycle time, we propose a new energy mechanism belonging to the second approach. The key element in this mechanism is a one-way bearing.

Fig. 7 illustrates the energy mechanism. A rotation link is connected to the output shaft of a speed reduction system via a one-way bearing not shown in the figure. Because of the one-way

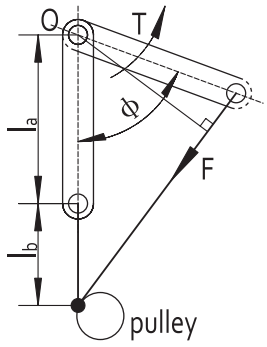

Fig. 8. Statics for the energy mechanism.

bearing, the rotation link can only rotate in the counterclockwise direction. A cable, which is guided by two pulleys, connects the end of rotation link to the robot's foot. If the rotation link rotates from the bottom vertical initial position, the cable forces the body to move toward the foot [see Fig. 7(a)]. The rotation link's top vertical position [see Fig. 7(b)] is a critical position since the torque resulted from the cable will switch its direction. Once the link passes this position, the energy is released, and the body accelerates upward [see Fig. 7(c)]. The body and foot in Fig. 7 are the same parts in the jumping mechanism shown in Fig. 6(a), but the links are not shown for a clear view.

With such a mechanism, the force F in Fig. 6(a) can be applied for energy charge. For the optimization in Section IV, we perform the static analysis for the rotation link to relate this force to the torque generated by the speed reduction system. As shown in Fig. 8, l_a is the length of the rotation link, and l_b is the vertical distance from the end of the rotation link to the pulley's center. If the link is rotated to a new position shown as the dashed line in the figure with a rotation angle $\phi \in [0, \pi]$, then the required torque T is equal to the torque generated by F with respect to pivot point O:

$$T = \frac{F l_a (l_a + l_b) \sin\phi}{\sqrt{l_a^2 + (l_a + l_b)^2 - 2 l_a (l_a + l_b) \cos\phi}}. \tag{15}$$

For the optimization in Section IV, we also represent the vertical distance y between the body and the foot shown in Fig. 6(a) as

$$y = y_{\max} - (\sqrt{l_a^2 + (l_a + l_b)^2 - 2 l_a (l_a + l_b) \cos\phi} - l_b) \tag{16}$$

C. Self-Righting Mechanism

With the jumping and energy mechanisms, the robot can jump if it initially stands on the ground with its foot. This case, however, seldom happens due to the landing impact. Therefore, a self-righting mechanism is needed to make the robot recover from possible landing postures.

In general, there are two methods for self-righting. The first one is the passive recovery based on the center of gravity (CoG). The robot will stand up if the CoG is sufficiently close to the foot. Examples include the EPFL jumper V3 [21], the Jollbot [30], and our first robot [23]. The second method, which is widely used in animals, is the active recovery with actuated parts. For instance, the beetles employ their legs for self-righting [52],

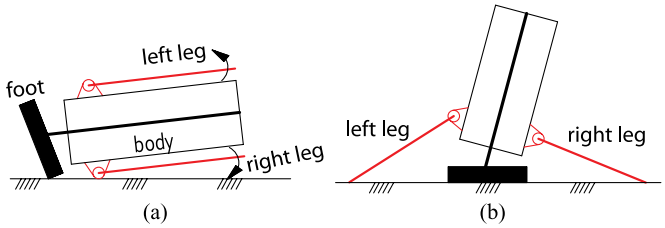

Fig. 9. Self-righting mechanism. (a) Initial position after the robot lands on the ground. (b) Final position when the robot stands up.

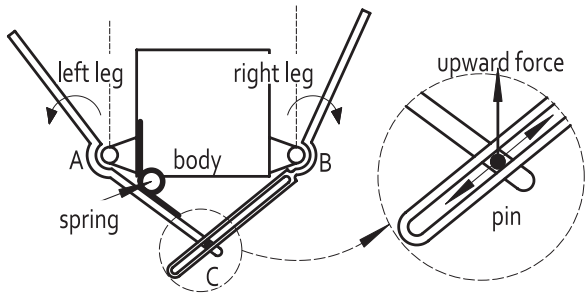

Fig. 10. Details of the self-righting mechanism.

while the turtles utilize the head because of their short legs [53]. The active recovery is implemented in the frogbot [3] and the new surveillance robot [11]. For our robot, we adopt the active self-righting to achieve a small robot size.

Fig. 9 illustrates the working principle for our self-righting mechanism. The robot has a rectangular shape with two surfaces significantly larger than the other four. As a result, the robot will contact the ground with one of these two large surfaces most of the time after landing. Without loss of generality, we assume a landing posture as shown in Fig. 9(a). Two self-righting legs on the body are initially parallel to the two large surfaces. Once actuated, they can rotate simultaneously in opposite directions. After a certain amount of rotation, the robot can stand up for the next jump. The final position when both legs are fully extended is shown in Fig. 9(b).

The detailed mechanism is shown in Fig. 10, where the whole mechanism is shown on the left and a partial enlargement is shown on the right. Note that the foot is not shown for a clear view. A revolute joint connects each leg to the body. A pin (shown to be a solid circle in the enlargement) fixed to the left leg can slide along a groove in the right leg. This way, if we apply an upward force on the pin, both legs will rotate but in opposite directions. A small torsion spring—with one end fixed to the body and the other end attached to the left leg—will make both legs return to their original positions if the upward force is removed.

We apply the upward force in Fig. 10 using the same actuator for energy charge. In fact, the body moves toward the foot during the energy charge process. With this motion, if a protrusion is attached to the foot and beneath the pin, the upward force will be generated once the protrusion contacts the pin. If the energy is released, the body will move away from the foot; consequently, the upward force is removed when the body is a certain distance away from the foot.

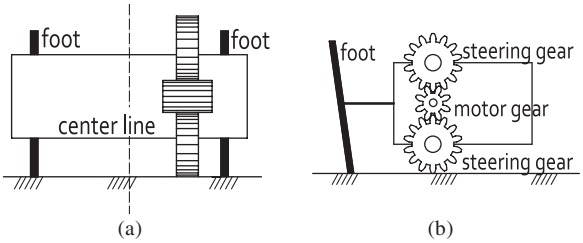

Fig. 11. Steering mechanism. (a) Front view. (b) Side view.

From the aforementioned discussions, the energy charge and the self-righting can be performed simultaneously, which leads to a short cycle time. Furthermore, all the motion can be accomplished with the motor's one-directional rotation. Note that the frogbot also employs a single motor for the energy charge and the self-righting. The self-righting process, however, is divided into two phases due to the shape of the robot [3].

D. Steering Mechanism

The final mechanism to realize the motion sequence in Fig. 2 is the steering mechanism, which can change the jumping direction. A review of steering methods for jumping robot can be found in [21]. Based on our robot's rectangular shape, we propose a steering method without extra actuators.

The steering mechanism is illustrated in Fig. 11. Two steering gears are placed symmetrically about the motor gear. Both gears are a certain distance away from the robot's centerline. Since the robot contacts the ground with one of its two large surfaces after landing, one of the two steering gears will touch the ground. Therefore, if the motor rotates, the robot will change its heading direction.

The same motor for the other three mechanisms actuates the steering mechanism. In fact, the steering mechanism is driven by the motor's one-directional rotation, while the other three mechanisms are actuated by the other directional rotation. One steering gear is also used in the speed reduction system for energy charge. If the motor rotates in one direction, this gear is used for energy charge. If the motor rotates in the other direction, the rotation link in Fig. 7 will not rotate due to the one-way bearing. In this case, this gear can steer the robot.

The steering mechanism is improved from our previous design in [46], where a single large gear at the end of speed reduction system is the steering gear. Because of its large diameter, the gear can touch the ground no matter which large surface of the robot contacts the ground. This method, although simpler, has a slow steering speed due to the large gear's small angular velocity. The new design increases the speed because the two steering gears are next to the motor gear, resulting in a large angular velocity.

IV. Design Optimization

Based on the analysis in Section III, the mechanism dimensions can be determined through optimization. In this section, we optimize the jumping mechanism together with the energy mechanism to obtain the smallest peak torque for energy charge.

TABLE I
List of Parameters for Optimization

l_2	length of the upper link (Fig. 6(a))
l_3	length of the lower link (Fig. 6(a))
l_d	difference between the body link l_1 and the foot link l_4
l_a	length of the rotation link (Fig. 8)
l_b	vertical distance from the rotation link to the pulley (Fig. 8)
y	vertical distance between the body and the foot (Fig. 6(a))
α	angle between the body link and the upper link (Fig. 6(a))
β	angle between the foot link and the lower link (Fig. 6(a))
ϕ	angle between the rotation link and the vertical line (Fig. 8)
E_0	total energy stored in the spring
k	torsion spring constant

After that, the dimensions of the self-righting mechanism are derived based on practical requirements. The steering mechanism is not discussed because it is determined by the energy mechanism.

A. Jumping Mechanism and Energy Mechanism

With the jumping and energy mechanisms, if the same energy can be charged with a small peak value of torque T generated by the speed reduction system, then the weight and size for the robot can be reduced. Therefore, optimization is needed to minimize the peak value of T.

In the following, we perform the optimal design in four steps: identifying the optimization variables, formulating the objective function, obtaining the constraints, and solving the constrained optimization problem. For easy reference, the parameters used in the optimization are listed in Table I.

To identify the optimization variables, we substitute the force equation (11) into the torque equation (15)

$$T = \frac{2kl_a(l_a+l_b)\sin\phi[l_3(\pi-2\alpha)\sin\beta + l_2(\pi-2\beta)\sin\alpha]}{l_2 l_3 \sin(\alpha+\beta)\sqrt{l_a^2+(l_a+l_b)^2-2l_a(l_a+l_b)\cos\phi}} \tag{17}$$

from which there are eight parameters: k, l_a, l_b, α, β, l_2, l_3, and ϕ. Since α and β can be written to be a function of y, l_2, l_3, and l_d by substituting (12) into (13), the true parameters are k, l_a, l_b, y, l_2, l_3, l_d, and ϕ.

Among the eight parameters, the variables will be only l_b, l_2, l_3, l_d, and ϕ because k, l_a, and y are either constants or dependents on the variables. First, according to our previous design [46], the torsion springs are chosen to have a constant $k = 58.98$ N $\cdot$ mm/rad. Second, l_a can be obtained from l_2, l_3, and l_d. In fact, from the geometrical relation of the energy mechanism, we have $l_a = (y_{\max} - y_{\min})/2$. If l_2, l_3, and l_d are given, then $y_{\max}$ can be derived using (14). With $y_{\max}$ known, $y_{\min}$ can also be determined to ensure a desired initial energy E_0 can be stored in the springs. Third, once $y_{\max}$ and l_a are known, y can also be derived through (16) based on l_b and ϕ. From the previous arguments, T is only a function of l_b, l_2, l_3, l_d, and ϕ, and we denote it as $T(l_b,\, l_2,\, l_3,\, l_d,\, \phi)$. The optimization variables are only l_b, l_2, l_3, and l_d because ϕ will run from 0 to π during each energy charge cycle.

The initial energy E_0 is determined based on the simulations in Section II. To achieve 1 m jumping height with a 75° take-off angle, the initial energy should be 0.3 J, but to leave

enough margin, we let $E_0 = 0.4$ J. In addition, the zero energy configuration for the jumping mechanism corresponds to the configuration when $y = y_{\max}$. The α and β angles for such a configuration depend on the link lengths and can be derived using (12) and (13).

Having identified the optimization variables, we formulate the objective function. Given l_b, l_2, l_3, and l_d, a torque curve as ϕ running from 0 to π can be plotted. The goal is to find the optimal l_b, l_2, l_3, and l_d such that the peak torque in the curve is the minimum among all possible curves. Therefore, the objective function is the peak torque in the curve:

$$g(l_b, l_2, l_3, l_d) = \max_{\phi \in [0, \pi]} T(l_b, l_2, l_3, l_d, \phi). \tag{18}$$

The next step is to obtain the constraints for the optimization variables. The lengths of l_2 and l_3 should be large enough to hold the torsion springs, but they cannot be too large due to the size limit of the robot. Therefore, with practical considerations, assume 15 $\text{mm} \leq l_2, l_3 \leq 20$ mm. With similar implementation reasons, we can have other linear constraints for l_b and l_d, and the optimization can be formulated as

$$\begin{aligned} \text{minimize} \quad & g(l_b, l_d, l_2, l_3) \\ \text{subject to} \quad & 7 \leq l_b \leq 12, -5 \leq l_d \leq 5 \\ & 15 \leq l_2 \leq 20, 15 \leq l_3 \leq 20 \end{aligned} \tag{19}$$

where the omitted length unit is the millimeter.

To solve the constrained optimization problem, we apply the numerical method because the analytical expression for $g(l_b, l_d, l_2, l_3)$ cannot be obtained. The optimization is realized by a dense discretization of ϕ and value evaluations at the resulting points [54]. The constrained nonlinear multivariable function in the Optimization Toolbox of MATLAB is employed to find the optimal value. Since the method can only obtain the local minimum, we choose various random initial points to run the optimization. The smallest objective function among these local minima is the optimal value, and the optimal dimensions are $l_b = 7$ mm, $l_d = 1.2$ mm, $l_2 = 15$ mm, and $l_3 = 20$ mm. The other parameters can be calculated accordingly: $y_{\max} = 33.3$ mm, $y_{\min} = 11.7$ mm, and $l_a = 10.8$ mm. To avoid interference between the two revolute joints at the foot, let $l_1 = 18$ mm; then, $l_4 = l_1 + l_d = 19.2$ mm.

To investigate how the variables affect the objective function, we plot the graphs showing the objective function and the variables. Since it is impossible to include the four variables into one graph, we divide them into two groups: l_b and l_d; l_2 and l_3. Fig. 12(a) shows how the objective function changes with respect to l_b and l_d by fixing l_2 and l_3 to the optimal value. As seen in the figure, the minimum value happens when l_b is the smallest and when l_d is in the middle part. Fig. 12(b) shows how the objective function varies with respect to l_2 and l_3 by fixing l_b and l_d to the optimal value. In this figure, the minimum value happens at the left corner. From these two figures, we see that the optimal dimensions obtained from the optimization are correct.

With the optimal design, we can obtain the torque curve with respect to the angle ϕ as shown in Fig. 13. From the figure, the torque profile is nonlinear with the peak value happening at $\phi = 66^\circ$. Furthermore, the torque is zero when the energy is about to be released ($\phi = 180^\circ$), which means the release of the energy requires the minimal torque. With the small torque during the release, the mechanism can reduce the probability of premature take-off [3]; consequently, it is highly possible that all the energy stored in the spring can be converted to the kinetic energy for take-off.

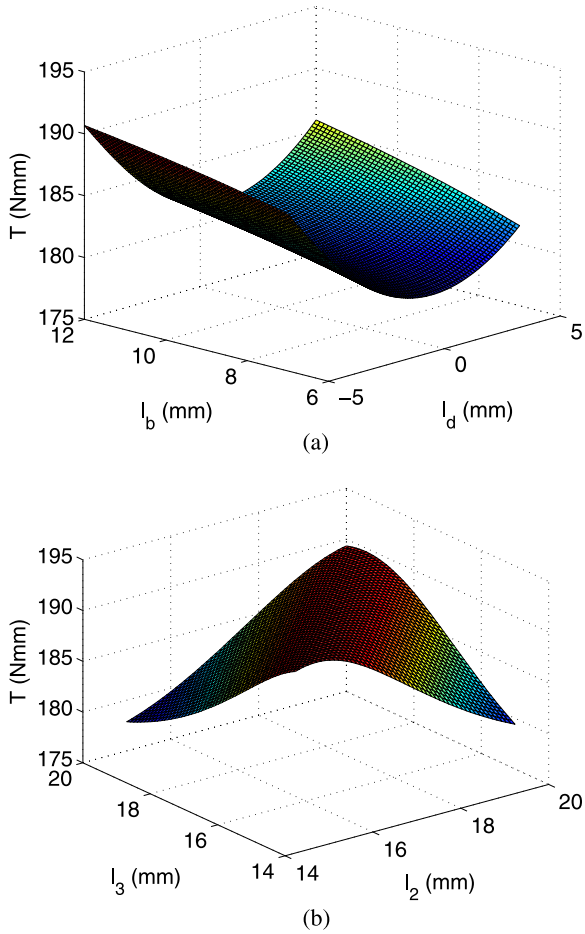

Fig. 12. Objective function varies with optimization variables: (a) variation of $g(l_b, l_d, l_2, l_3)$ with fixed l_2 and l_3 and (b) variation of $g(l_b, l_d, l_2, l_3)$ with fixed l_b and l_d.

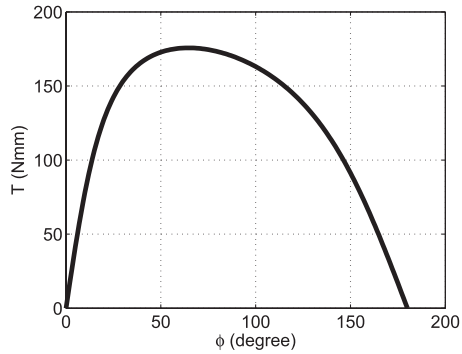

Fig. 13. Torque profile with the optimal dimensions.

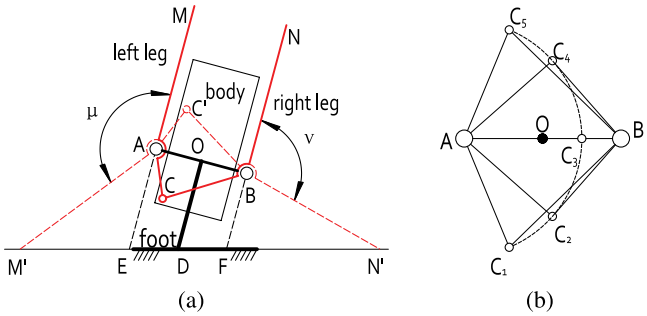

Fig. 14. Dimension design of the self-righting mechanism. (a) Mechanism with initial and final positions for both self-righting legs. (b) Simplification of the mechanism to determine the length for link AC.

B. Self-Righting Mechanism

The dimensions for the self-righting mechanism are critical for successful recovery from possible landing postures. The design variables include the leg length and the range of leg rotation angle. The initial and final positions for both recovery legs are shown in Fig. 14(a). The initial positions, AM and BN, are parallel to the body, and the final positions, AM′ and BN′, contact the ground with leg ends M' and N'. The ranges of leg rotation angle are denoted by μ and ν for the left and right leg, respectively. O is the middle point for AB. Moreover, we have AB $\perp$ OD and $\angle$ODN′ $= \theta = 75^\circ$, which is the robot take-off angle. The relation between the leg length and the range of leg rotation angle can be obtained using the law of sines in $\triangle$AM′E and $\triangle$BN′F:

$$\frac{|\mathrm{AM}'|}{\sin(\pi-\theta)} = \frac{|\mathrm{OD}|+|\mathrm{AO}|\tan(\pi/2-\theta)}{\sin(\mu-\pi+\theta)} \tag{20}$$

$$\frac{|\mathrm{BN}'|}{\sin\theta} = \frac{|\mathrm{OD}|-|\mathrm{BO}|\tan(\pi/2-\theta)}{\sin(\nu-\theta)}. \tag{21}$$

From (20) and (21), if μ or ν is large, then the leg length AM′ or BN′ can be small. To simplify the design, we fix $\mu = 135^\circ$ and $\nu = 105^\circ$ to let $\mu - \angle\mathrm{ODM}' = \nu - \angle\mathrm{ODN}' = 30^\circ$. With μ and ν fixed, $|\mathrm{AM}'|$ and $|\mathrm{BN}'|$ can be solved from (20) and (21) given $|\mathrm{AO}| = |\mathrm{BO}|$ and $|\mathrm{OD}|$, which are determined from the implementation.

The next step is to design the length of AC shown in Fig. 14(a) to achieve the desired angle ranges. Without the body, the foot, the part AM in the left leg, and the part BN in the right leg, the mechanism can be simplified as shown in Fig. 14(b). In the figure, C_1 to C_5 are different locations for the end point C of link AC. C_1 and C_5, symmetric with respect to AB, are the limit position for link AC; therefore, $\angle\mathrm{C}_1\mathrm{AC}_5 = \mu = 135^\circ$. C_2 and C_4, symmetric with respect to AB as well, are the tangent points from point B to the circle formed by link AC. Since BC_2 and BC_4 are the limit positions for link BC, $\angle\mathrm{C}_2\mathrm{BC}_4 = \nu = 105^\circ$. From right-angled $\triangle\mathrm{ABC}_4$, we have $|\mathrm{AC}| = |\mathrm{AB}|\sin(\nu/2)$. The parameters for the right leg can also be derived accordingly.

V. Fabrication and Experimental Results

A. Fabrication and Development

The solid model for the robot is shown in Fig. 1(b), and the individual mechanisms are shown from Fig. 15(a) to (d). Some parts appear in multiple figures because they are used in different mechanisms. We elaborate on the implementation for each mechanism in this section.

For the jumping mechanism shown in Fig. 15(a), both the left-hand (9287K77 from McMaster-Carr) and the right-hand (9287K26 from McMaster-Carr) torsion springs are required. We use a pin-hole structure to implement the revolute joints. The torsion springs are held in place by the pins of the revolute joints. The bottom of the foot is designed with a tilted angle 15° to provide the 75° take-off angle.

The major part of the energy mechanism, shown in Fig. 15(b), is the motor-actuated gear train or speed reduction system. The gear train has three stages consisting of a motor gear (eight teeth), a compound gear (28/8 teeth), another compound gear (28/9 teeth), and a spur gear (35 teeth). Therefore, the total speed reduction ratio is 47.6. Based on this ratio and the required peak torque (178 N · mm) in Fig. 13, the motor (GH810136V3 from Gizmoszone) with a stall torque 8 N · mm is chosen. For this motor, a sufficient margin has been left to overcome the friction in the gear train. The one-way bearing (kit8637 from VXB bearings) cannot be shown in Fig. 15(b) because it is inside the rotation link.

Fig. 15(c) shows a section view of the self-righting mechanism. The revolute joints connecting the two legs to the body are achieved by the pin-hole structure as well. The pusher attached to the foot—not shown in Fig. 15(c)—can provide the upward force in Fig. 10. The small torsion spring (9287K12 from McMaster-Carr) is held in placed by the pin in the left revolute joint.

The steering mechanism, shown in Fig. 15(d), comes from the energy mechanism. All of the gears in the gear train of Fig. 15(b) are shown in Fig. 15(d). Only the right steering gear does not belong to the energy mechanism, and the left steering gear is part of the gear train to charge energy.

We obtain the robot parts from three sources. First, some parts are off-the-shelf components such as springs and bearings. Second, most of the other parts are fabricated using the selective laser sintering with the DuraForm HST material. It has a density only 1.20 g/cm^3, yet it can be used for functional prototypes. Third, the aluminum shafts in the gear train are manufactured using traditional machining methods.

The robot is powered by a FullRiver 50 mAh LiPo battery with an average 3.7 V output. Since the energy mechanism is placed on the right side of the body, the battery—shown in Fig. 1(b)—is placed on the left side to balance the robot's weight.

For the robot, the mass and the initial stored energy are needed to obtain the theoretical performances. The lower part of the robot contains the components below the revolute joint connecting the lower link to the upper link, while the upper part includes all of the other components above that joint. The mass for each part is $m_1 = 5.4$ g and $m_2 = 18.1$ g. The initial energy E_0 is designed to be 0.4 J, but the true energy cannot be this

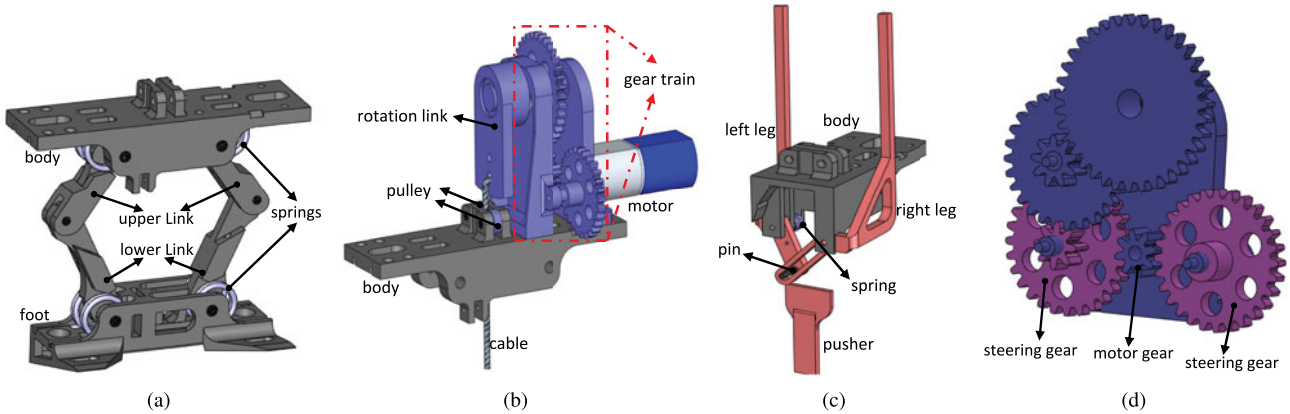

Fig. 15. Solid model for each mechanism. (a) Jumping mechanism [principle shown in Fig. 6(a)]. (b) Energy mechanism (principle shown in Fig. 7). (c) Self-righting mechanism (principle shown in Fig. 10). (d) Steering mechanism (principle shown in Fig. 11).

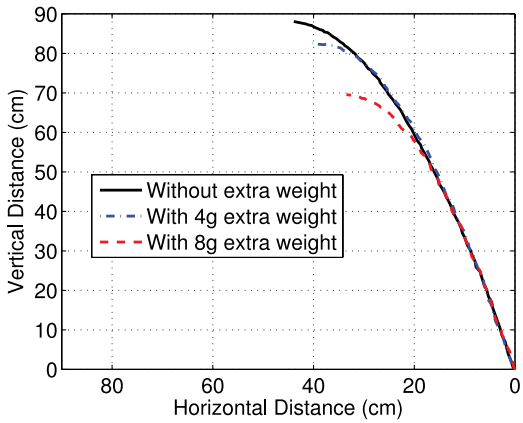

Fig. 16. Jumping experimental results: average trajectories for three sets of experiments.

TABLE II
EXPERIMENTAL AND THEORETICAL JUMPING PERFORMANCES

Extra Weight	Experimental Height (cm)	Experimental Distance (cm)	Estimated Height (cm)	Estimated Distance (cm)
$0g$	87.2 ± 2.2	89.8 ± 4.0	97.9	103.4
$4g$	82.1 ± 1.2	80.6 ± 1.6	88.9	94.2
$8g$	69.5 ± 2.2	67.8 ± 2.8	81.1	86.1

much because the minimum distance $y_{\min}$ for y cannot be the designed value due to the cable's elasticity. Therefore, the true $y_{\min}$ is measured to calculate the energy stored in the spring. In fact, $y_{\min} = 14$ mm, and the resulting $E_0 = 0.34$ J.

B. Experimental Results

Jumping experiments are conducted to determine the jumping performances. To eliminate the slippage during the robot's take-off, we place the robot on a high coefficient of friction surface (fine-grained sand paper with a grit designation 320). To obtain the performances, we also place the robot in front of a board with small holes. The distance between neighboring holes, either horizontal or vertical, is 1 in (2.54 cm). When the robot jumps, a video is recorded by a Casio Exilim EX-FH25 high-speed camera with a frame rate 240 frames/s. After that, the jumping height is obtained offline from the video by comparing the robot's highest position with the vertical holes, while the jumping distance is obtained by comparing the landing position with the horizontal holes. Detailed jumping experiments can be found in the accompanying video attachment for this paper.

Five jumps are carried out to obtain the average jumping performance. The average jumping trajectory for these five jumps is plotted with the solid line in Fig. 16. Note that the robot jumps from the right to the left, and only half of the trajectory is shown due to the symmetry of the trajectory. The average performance is listed in Table II, where the robot can jump 87.2 cm in height and 89.8 cm in distance. The standard deviations for these jumps

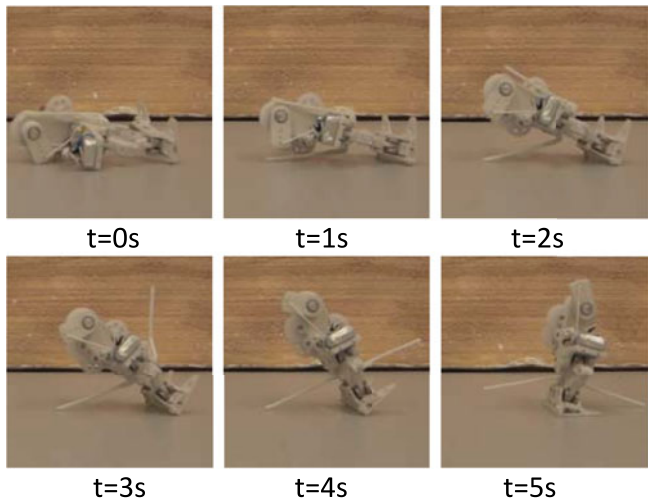

Fig. 17. Self-righting experimental result. Six individual frames extracted from a self-righting video.

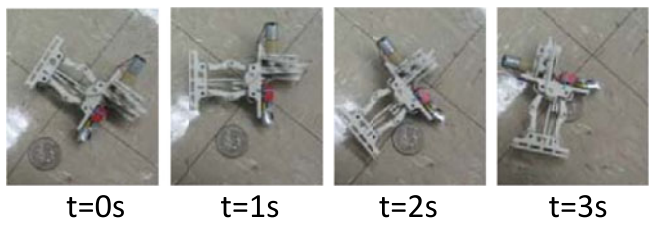

Fig. 18. Steering experimental result. Four individual frames extracted from a steering video.

TABLE III
COMPARISON WITH EXISTING ROBOTS WITH THE JUMPING ABILITY

Robot Name	Mass [g]	Size [cm]	Charge time [s]	Jumping height [cm]	Jumping distance [cm]	Normalized jumping height [cm]	Height per mass and size [10·cm·/(g·cm)]	Self-righting	Steering	Onboard energy	Actuation
Flea robot [2]	1.1	2	15	64	70	68.8	312.73	no	no	no	3 SMA
Frogbot [3]	1300	15	30	90	200	117.8	0.06	yes	yes	yes	1 motor
Surveillance robot [11]	150	12.2	60	105	60	107.1	0.59	yes	no	yes	2 motors
Grillo III [17]	22	5	8	10	20	12.5	1.14	no	no	yes	1 motor
EPFL jumper V1 [19]	6.98	5	3.5	138	79	140.8	40.34	no	no	yes	1 motor
EPFL jumper V2 [20]	9.8	12	3.5	76	81	81.4	6.92	yes	no	yes	1 motor
EPFL jumper V3 [21]	14.33	18	3.5	62	46	64.1	2.49	yes	yes	yes	2 motors
Multimodal robot [22]	72	×	×	170	0	170	×	no	no	yes	×
Compact jumping robot [27]	18	11	0.3	15	95	52.6	2.66	no	no	no	2 motors
MIT microbot [29]	46	10	×	38	0	38	0.83	no	no	no	1 DEA
Jollbot [30]	465	30	1.44	18.4	0	18.4	0.01	yes	yes	yes	2 motors
Deformable robot [31]	5	9	45	18	0	18	4	yes	no	no	4 SMA
MSU jumper	**23.5**	**6.5**	**10**	**87.2**	**89.8**	**93.0**	**6.09**	**yes**	**yes**	**yes**	**1 motor**

× Data are not available from the reference.

are 2.2 and 4.0 cm for the height and distance, respectively. The take-off velocity can also be obtained as 4.3 m/s. Therefore, the jumping efficiency—defined as the ratio between the kinetic energy before robot's take-off E and the initial stored energy E_0—is 63.0%.

The sensor network application requires the robot to be able to carry payloads for extra sensors. Therefore, experiments are conducted to investigate the jumping performance with an extra weight. The extra weight is placed on the opposite side of gear train to balance the robot's weight. The average performances for five jumps are listed in Table II as well, and the average trajectories are also shown in Fig. 16. For an extra 4 g mass, the average jumping height and distance are 82.1 and 80.6 cm, respectively. If an extra 8 g mass is added, then the average jumping height and distance become 69.5 and 67.8 cm, respectively. The small decreases in both the jumping height and distance indicate that the robot can carry some payloads without degrading its performance significantly.

The theoretical performances with the air resistance are also listed in Table II. From the table, the experimental results are worse than the theoretical calculations. The major reason for such a discrepancy is the friction in the jumping mechanism. In particular, the friction exists in all of the revolute joints since they are built using the pin-hole structure. Because of the friction, only part of the stored energy is converted to the kinetic energy for take-off. Additionally, some energy is also transformed to the robot's rotation energy in the air. This energy loss, however, is negligible because of the robot's small moment of inertia and angular velocity.

The self-righting experiments are also carried out. One of the results is shown in Fig. 17, where six frames from a video recording the self-righting process are presented. The robot needs 5 s for self-righting as seen from the time under each picture. Since the self-righting process is performed simultaneously with the energy charge process, the cycle time does not increase. Additional results on an uneven plane (the top of a rock) can be found in the accompanying video.

The steering experiments are performed on the ground as well. Four frames from a video are shown in Fig. 18. In this experiment, the robot changes its direction in the counterclockwise direction. From the video, the robot can rotate 360° in about 10 s; therefore, the rotation speed is about 36°/s, which is much faster than the 2°/s for our previous design [46]. Supplemental steering experiments on an uneven plane (the top of a rock) are also shown in the accompanying video.

C. Comparison With Other Robots

Comparisons with other jumping robots are listed in Table III. Since robots with different energy storage methods have different characteristics, only the robots based on traditional and customized springs are listed. Furthermore, some robots are not included because they use wheels as the primary locomotion method.

To make the comparison fair, appropriate indices should be chosen. The mass, size, jumping height, and jumping distance are usually selected for comparison [30]. In Table III, these four indices are listed in column two, three, five, and six, respectively. Note that the size is the maximum dimension among the length, width, and height. For spring-based robots, the charge time—shown in the fourth column in the table—is also an important index since more energy can be stored with a longer charge time provided the other conditions are the same. Since the jumping height and distance vary with take-off angles, the normalized jumping height with a 90° take-off angle is calculated from the jumping height and distance using (3) and (4). This index is the seventh column in the table. To compare the obstacle height that the robot can overcome given its size and weight [9], the height per mass and size is listed in the eighth column. It is obtained from dividing the normalized jumping height by the mass and the size. The subsequent three columns indicate whether the robot has self-righting, steering, and onboard energy, respectively. Finally, the type and the number of actuators are listed in the last column.

Compared with the robots in Table III, the MSU jumper has a good overall performance among those robots with the continuous steerable jumping ability. The overall performance is indicated by the height per mass and size index (the eighth column in Table III). Besides the good overall jumping performance, the MSU jumper employs a single motor for continuous steerable jumping. Except the frogbot and those robots with different actuation methods, all of the other robots need extra

motor to achieve either self-righting or steering, as indicated in the last column of Table III.

Compared with the MSU jumper, the other jumping robots have their own merits as well. First, the robots with wheels can run faster if no obstacle exists [13], [25]. Second, the robots with a sphere structure for self-righting can roll passively on the ground. Moreover, the enclosed sphere protects the robot from damage [20], [21], [30]. Third, some robots have the embedded sensing, control, and communication system [3], [11]. With such a system, the control, navigation, and motion planning can be investigated for the jumping locomotion [55].

VI. Conclusion

To facilitate the locomotion for mobile sensors in environments with obstacles, this paper presents the mechanical design of a miniature steerable jumping robot. Different from existing designs, the robot can satisfy three design requirements: continuous steerable jumping, minimum actuation, and light weight. Moreover, optimal design is performed to obtain the best mechanism dimensions. Experimental results show that the robot has a good overall jumping performance compared with existing jumping robots. The jumping robot described in this paper can be potentially used in mobile sensor networks for various applications. Furthermore, the design method presented in this paper may also be applied to other miniature robot designs. Future work will focus on the embedded control system to make the robot an autonomous jumping sensor node.

References

[1] A. Krause, C. Guestrin, A. Gupta, and J. Kleinberg, "Near-optimal sensor placements: Maximizing information while minimizing communication cost," in *Proc. Int. Conf. Inf. Process. Sens. Netw.*, Nashville, TN, USA, 2006, pp. 2–10.

[2] M. Noh, S.-W. Kim, S. An, J.-S. Koh, and K.-J. Cho, "Flea-inspired catapult mechanism for miniature jumping robots," *IEEE Trans. Robot.*, vol. 28, no. 5, pp. 1007–1018, Oct. 2012.

[3] J. Burdick and P. Fiorini, "Minimalist jumping robots for celestial exploration," *Int. J. Robot. Res.*, vol. 22, no. 7, pp. 653–674, 2003.

[4] S. Bergbreiter, "Effective and efficient locomotion for millimeter-sized microrobots," in *Proc. IEEE/RSJ Int. Conf. Intell. Robots Syst.*, Nice, France, 2008, pp. 4030–4035.

[5] F. Cintrón, K. Pongaliur, M. Mutka, and L. Xiao, "Energy balancing hopping sensor network model to maximize coverage," in *Proc. 18th Int. Conf. Comput. Commun. Netw.*, San Francisco, CA, USA, 2009, pp. 1–6.

[6] F. Cintrón, K. Pongaliur, M. W. Mutka, L. Xiao, J. Zhao, and N. Xi, "Leveraging height in a jumping sensor network to extend network coverage," *IEEE Trans. Wireless Commun.*, vol. 11, no. 5, pp. 1840–1849, May 2012.

[7] S. Bergbreiter, "Autonomous jumping microrobots," Ph.D. dissertation, Dept. Electr. Eng. Comput. Sci., Univ. California, Berkeley, USA, Dec. 2007.

[8] R. Armour, "A biologically inspired jumping and rolling robot," Ph.D. dissertation, Dept. Mech. Eng., Univ. Bath, Bath, U.K., May 2010.

[9] M. Kovac, "Bioinspired jumping locomotion for miniature robotics," Ph.D. dissertation, Swiss Federal Inst. Technol., Lausanne, Switzerland, Jun. 2010.

[10] G. Song, K. Yin, Y. Zhou, and X. Cheng, "A surveillance robot with hopping capabilities for home security," *IEEE Trans. Consum. Electron.*, vol. 55, no. 4, pp. 2034–2039, Nov. 2009.

[11] J. Zhang, G. Song, G. Qiao, T. Meng, and H. Sun, "An indoor security system with a jumping robot as the surveillance terminal," *IEEE Trans. Consum. Electron.*, vol. 57, no. 4, pp. 1774–1781, Nov. 2011.

[12] L. Bai, W. Ge, X. Chen, and R. Chen, "Design and dynamics analysis of a bio-inspired intermittent hopping robot for planetary surface exploration," *Int. J. Adv. Robot. Syst.*, P. Gonzalez-De-Santos, L. Nalpantidis, and A. Barrera, Eds., ISBN: 17298806, InTech, DOI: 10.5772/51930.

[13] B. G. A. Lambrecht, A. D. Horchler, and R. D. Quinn, "A small, insect inspired robot that runs and jumps," in *Proc. IEEE Int. Conf. Robot. Autom.*, Barcelona, Spain, 2005, pp. 1240–1245.

[14] E. Dupuis, S. Montminy, M. Farhad, and H. Champliaud, "Mechanical design of a hopper robot for planetary exploration," in *Proc. 9th ESA Worksh. Adv. Space Technol. Robot. Autom.*, ESTEC, Netherlands, ASTRA 2006, Nov. 28–30, 2006.

[15] U. Scarfogliero, C. Stefanini, and P. Dario, "Design and development of the long-jumping "grillo" mini robot," in *Proc. IEEE Int. Conf. Robot. Autom.*, Roma, Italy, 2007, pp. 467–472.

[16] U. Scarfogliero, C. Stefanini, and P. Dario, "The use of compliant joints and elastic energy storage in bio-inspired legged robots," *Mech. Mach. Theory*, vol. 44, no. 3, pp. 580–590, 2009.

[17] F. Li, W. Liu, X. Fu, G. Bonsignori, U. Scarfogliero, C. Stefanini, and P. Dario, "Jumping like an insect: Design and dynamic optimization of a jumping mini robot based on bio-mimetic inspiration," *Mechatronics*, vol. 22, no. 2, pp. 167–176, 2012.

[18] K. Kikuchi, K. Sakaguchi, T. Sudo, N. Bushida, Y. Chiba, and Y. Asai, "A study on a wheel-based stair-climbing robot with a hopping mechanism," *Mech. Syst. Signal Process.*, vol. 22, no. 6, pp. 1316–1326, 2008.

[19] M. Kovac, M. Fuchs, A. Guignard, J. Zufferey, and D. Floreano, "A miniature 7g jumping robot," in *Proc. IEEE Int. Conf. Robot. Autom.*, Pasadena, CA, 2008, pp. 373–378.

[20] M. Kovac, M. Schlegel, J. Zufferey, and D. Floreano, "A miniature jumping robot with self-recovery capabilities," in *Proc. IEEE/RSJ Int. Conf. Intell. Robots Syst.*, St. Louis, MO, USA, 2009, pp. 583–588.

[21] M. Kovac, M. Schlegel, J. Zufferey, and D. Floreano, "Steerable miniature jumping robot," *Auton. Robots*, vol. 28, no. 3, pp. 295–306, 2010.

[22] M. A. Woodward and M. Sitti, "Design of a miniature integrated multimodal jumping and gliding robot," in *Proc. IEEE/RSJ Int. Conf. Intell. Robots Syst.*, San Francisco, CA, USA, 2011, pp. 556–561.

[23] J. Zhao, R. Yang, N. Xi, B. Gao, X. Fan, M. Mutka, and L. Xiao, "Development of a self-stabilization miniature jumping robot," in *Proc. IEEE/RSJ Int. Conf. Intell. Robots Syst.*, St. Louis, MO, USA, 2009, pp. 2217–2222.

[24] J. Zhao, N. Xi, B. Gao, M. Mutka, and L. Xiao, "Design and testing of a controllable miniature jumping robot," in *Proc. IEEE/RSJ Int. Conf. Intell. Robots Syst.*, Taipei, Taiwan, 2010, pp. 3346–3351.

[25] S. A. Stoeter and N. Papanikolopoulos, "Kinematic motion model for jumping scout robots," *IEEE Trans. Robot. Autom.*, vol. 22, no. 2, pp. 398–403, Apr. 2006.

[26] A. Yamada, M. Watari, H. Mochiyama, and H. Fujimoto, "An asymmetric robotic catapult based on the closed elastica for jumping robot," in *Proc. IEEE Int. Conf. Robot. Autom.*, Pasadena, CA, USA, 2008, pp. 232–237.

[27] A. Yamada, M. Watari, H. Mochiyama, and H. Fujimoto, "A compact jumping robot utilizing snap-through buckling with bend and twist," in *Proc. IEEE/RSJ Int. Conf. Intell. Robots Syst.*, Taipei, Taiwan, 2010, pp. 389–394.

[28] S. Kesner, J. Plante, P. Boston, and S. Dubowsky, "A hopping mobility concept for a rough terrain search and rescue robot," in *Proc. Int. Conf. Climb. Walk. Robots Support. Technol. Mobile Mach.*, 2007, Singapore, pp. 271–280.

[29] S. Dubowsky, S. Kesner, J. Plante, and P. Boston, "Hopping mobility concept for search and rescue robots," *Ind. Robot*, vol. 35, no. 3, pp. 238–245, 2008.

[30] R. Armour, K. Paskins, A. Bowyer, J. Vincent, and W. Megill, "Jumping robots: A biomimetic solution to locomotion across rough terrain," *Bioinsp. Biomim.*, vol. 2, no. 3, pp. 65–82, 2007.

[31] Y. Sugiyama and S. Hirai, "Crawling and jumping by a deformable robot," *Int. J. Robot. Res.*, vol. 25, no. 5–6, pp. 603–620, 2006.

[32] Y. Matsuyama and S. Hirai, "Analysis of circular robot jumping by body deformation," in *Proc. IEEE Int. Conf. Robot. Autom.*, Rome, Italy, 2007, pp. 1968–1973.

[33] T. Ho and S. Lee, "A shape memory alloy-actuated bio-inspired mesoscale jumping robot," *Int. J. Adv. Robot. Syst.*, vol. 9, no. 91, 2012.

[34] H. Tsukagoshi, M. Sasaki, A. Kitagawa, and T. Tanaka, "Design of a higher jumping rescue robot with the optimized pneumatic drive," in *Proc. IEEE Int. Conf. Robot. Autom.*, Barcelona, Spain, 2005, pp. 1276–1283.

[35] E. Watari, H. Tsukagoshi, A. Kitagawa, and T. Tanaka, "A higher casting and jump motions realized by robots using magnetic brake cylinder," *J. Mech. Robot.*, vol. 3, no. 4, pp. 041002-1–041002-11, 2011, doi:10.1115/1.4004889.

[36] D. H. Kim, J. H. Lee, I. Kim, S. H. Noh, and S. K. Oho, "Mechanism, control, and visual management of a jumping robot," *Mechatronics*, vol. 18, no. 10, pp. 591–600, 2008.
[37] F. Kikuchi, Y. Ota, and S. Hirose, "Basic performance experiments for jumping quadruped," in *Proc. IEEE/RSJ Int. Conf. Intell. Robots Syst.*, Las Vegas, NV, USA, 2003, pp. 3378–3383.
[38] T. Tanaka and S. Hirose, "Development of leg-wheel hybrid quadruped airhopper: Design of powerful light-weight leg with wheel," in *Proc. IEEE Int. Conf. Robot. Autom.*, Pasadena, CA, USA, 2008, pp. 3890–3895.
[39] R. Niiyama, A. Nagakubo, and Y. Kuniyoshi, "Mowgli: A bipedal jumping and landing robot with an artificial musculoskeletal system," in *Proc. IEEE Int. Conf. Robot. Autom.*, Rome, Italy, 2007, pp. 2546–2551.
[40] R. Hayashi and S. Tsujio, "High-performance jumping movements by pendulum-type jumping machines," in *Proc. IEEE/RSJ Int. Conf. Intell. Robots Syst.*, Maui, HI, USA, 2001, pp. 722–727.
[41] J. German. (2000). "Hop to it: Sandia hoppers leapfrog conventional wisdom about robot mobility," [Online]. Available: http://www.sandia.gov/LabNews/LN10-20-00/hop_story.html
[42] E. Ackerman, "Boston dynamics sand flea robot demonstrates astonishing jumping skills," IEEE Spectrum Robot. Blog, Mar. 2012.
[43] S. Bergbreiter and K. Pister, "Design of an autonomous jumping microrobot," in *Proc. IEEE Int. Conf. Robot. Autom.*, Rome, Italy, 2007, pp. 447–453.
[44] W. A. Churaman, A. P. Gerratt, and S. Bergbreiter, "First leaps toward jumping microrobots," in *Proc. IEEE/RSJ Int. Conf. Intell. Robots Syst.*, San Francisco, CA, USA, 2011, pp. 1680–1686.
[45] P. Zhang and Q. Zhou, "Voice coil based hopping mechanism for microrobot," in *Proc. IEEE Int. Conf. Robot. Autom.*, Kobe, Japan, 2009, pp. 3001–3006.
[46] J. Zhao, N. Xi, B. Gao, M. Mutka, and L. Xiao, "Development of a controllable and continuous jumping robot," in *Proc. IEEE Int. Conf. Robot. Autom.*, Shanghai, China, 2011, pp. 4614–4619.
[47] R. M. Alexander, *Principles of Animal Locomotion*. Princeton, NJ, USA: Princeton Univ. Press, 2003.
[48] R. W. Fox, P. J. Pritchard, and A. T. McDonald, *Introduction to Fluid Mechanics*, 7th ed. New York, NY, USA: Wiley, 2008.
[49] A. M. Johnson, T. Libby, E. Chang-Siu, M. Tomizuka, R. J. Full, and D. E. Koditschek, "Tail assisted dynamic self righting," in *Proc. 15th Int. Conf. Climb. Walk. Robots*, Jul. 2012, pp. 611–620.
[50] H. C. Bennet-Clark and G. M. Alder, "The effect of air resistance on the jumping performance of insects," *J. Exp. Biol.*, vol. 82, no. 1, pp. 105–121, 1979.
[51] R. M. Alexander, "Leg design and jumping technique for humans, other vertebrates and insects," *Philos. Trans. R. Soc. Lond. B Biol. Sci.*, vol. 347, pp. 235–248, 1995.
[52] L. Frantsevich, "Righting kinematics in beetles (insecta: Coleoptera)," *Arthropod Struct. Development*, vol. 33, no. 3, pp. 221–235, 2004.
[53] G. Domokos and P. L. Várkonyi, "Geometry and self-righting of turtles," *Proc. Roy. Soc.: Biol. Sci.*, vol. 275, no. 1630, pp. 11–17, 2008.
[54] J. A. Carretero, R. P. Podhorodeski, M. A. Nahon, and C. M. Gosselin, "Kinematic analysis and optimization of a new three degree-of-freedom spatial parallel manipulator," *ASME J. Mech. Des.*, vol. 122, no. 1, pp. 17–24, 2000.
[55] Y. Pei, F. Cintrón, M. Mutka, J. Zhao, and N. Xi, "Hopping sensor relocation in rugged terrains," in *Proc. IEEE/RSJ Int. Conf. Intell. Robots Syst.*, 2009, pp. 3856–3861.

Jianguo Zhao (S'06) received the B.E. degree in mechanical engineering from Harbin Institute of Technology, Harbin, China, in 2005 and the M.E. degree in mechatronic engineering from Shenzhen Graduate School, Harbin Institute of Technology, Shenzhen, China, in 2007. He is currently working toward the Ph.D. degree with the Robotics and Automation Laboratory, Michigan State University, East Lansing, MI, USA.

His research interests include bio-inspired robotics, dynamics and control, visual servoing, control with limited information, and cyber physical systems.

Jing Xu (M'11) received the B.E. degree in mechanical engineering from Harbin Institute of Technology, Harbin, China, in 2003 and the Ph.D. degree in mechanical engineering from Tsinghua University, Beijing, China, in 2008.

From 2008 to 2010, he was a Postdoctor with the Department of Electrical and Computer Engineering, Michigan State University, East Lansing, MI, USA. He is currently an Associate Professor with the Department of Precision Instruments and Mechanology, Tsinghua University, Beijing, China. His research interests include robotics, manufacturing automation, and image processing.

Bingtuan Gao (M'10) received the B.E. degree in electrical engineering, the M.E. degree in control theory and control engineering, and the Ph.D. degree in power electronics and electrical drives, all from Harbin Institute of Technology, Harbin, China, in 2002, 2004, and 2007, respectively.

From 2008 to 2010, he was a Postdoctor with the Department of Electrical and Computer Engineering, Michigan State University, East Lansing, MI, USA. He is currently an Associate Professor with the School of Electrical Engineering, Southeast University, Nanjing, China. His research interests include robotics, manufacturing automation, and underactuated mechanical systems.

Ning Xi (F'07) received the D.Sc. degree in systems science and mathematics from Washington University, St. Louis, MO, USA, in 1993 and the B.S. degree in electrical engineering from the Beijing University of Aeronautics and Astronautics, Beijing, China.

He is the University Distinguished Professor and John D. Ryder Professor of Electrical and Computer Engineering with Michigan State University, East Lansing, MI, USA. He is also currently the Head and the Chair Professor of the Department of Mechanical and Biomedical Engineering, the City University of Hong Kong, Hong Kong. His research interests include robotics, manufacturing automation, micro/nano manufacturing, nano sensors and devices, and intelligent control and systems.

Fernando J. Cintrón (S'13) received the B.S. and M.E. degrees in computer engineering from the University of Puerto Rico, Mayagüez, Puerto Rico, in 2004 and 2007, respectively, and the Ph.D. degree from the Department of Computer Science and Engineering, Michigan State University, East Lansing, MI, USA.

His research interests include wireless networks, sensor networking, and mobile computing.

Matt W. Mutka (F'13) received the B.S. degree from the University of Missouri-Rolla, Rolla, MO, USA, the M.S. degree from Stanford University, Stanford, CA, USA, both in electrical engineering, and the Ph.D. degree in computer sciences from the University of Wisconsin-Madison, Madison, WI, USA.

He is on the faculty of the Department of Computer Science and Engineering, Michigan State University, East Lansing, MI, USA, where he is currently a Professor and Chairperson. He has been a Visiting Scholar with the University of Helsinki, Helsinki, Finland, and a Member of technical staff with Bell Laboratories, Denver, CO, USA. His current research interests include mobile computing, sensor networking, wireless networking, and multimedia networking.

Li Xiao (SM'10) received the B.S. and M.S. degrees in computer science from Northwestern Polytechnic University, Xi'an, China, and the Ph.D. degree in computer science from the College of William and Mary,Williamsburg, VA, USA.

She is an Associate Professor of Computer Science and Engineering with Michigan State University, East Lansing, MI, USA. Her research interests include distributed and networking systems, overlay systems and applications, and wireless networks.